Simple and accurate expressions for diffuse reflectance of semi-infinite and two-layer absorbing and scattering media

Dmitry Yudovsky and Laurent Pilon*

University of California, Los Angeles, Henry Samueli School of Engineering and Applied Science, Biomedical Engineering Inter-Departmental Program, Mechanical and Aerospace Engineering Department, Los Angeles, California 90095-1597, USA

*Corresponding author: pilon@seas.ucla.edu

Received 4 August 2009; revised 21 October 2009; accepted 26 October 2009; posted 27 October 2009 (Doc. ID 115203); published 1 December 2009

We present computationally efficient and accurate semiempirical models of light transfer suitable for real-time diffuse reflectance spectroscopy. The models predict the diffuse reflectance of both (i) semi-infinite homogeneous and (ii) two-layer media exposed to normal and collimated light. The two-layer medium consisted of a plane-parallel slab of finite thickness over a semi-infinite layer with identical index of refraction but different absorption and scattering properties. The model accounted for absorption and anisotropic scattering, as well as for internal reflection at the medium/air interface. All media were assumed to be nonemitting, strongly forward scattering, with indices of refraction between 1.00 and 1.44 and transport single-scattering albedos between 0.50 and 0.99. First, simple analytical expressions for the diffuse reflectance of the semi-infinite and two-layer media considered were derived using the two-flux approximation. Then, parameters appearing in the analytical expression previously derived were instead fitted to match results from more accurate Monte Carlo simulations. A single semiempirical parameter was sufficient to relate the diffuse reflectance to the radiative properties and thickness of the semi-infinite and two-layer media. The present model can be used for a wide range of applications including noninvasive diagnosis of biological tissue.

OCIS codes: 010.5620, 170.0170, 170.3660, 160.1190, 000.4430, 230.4170.

1. Introduction

Diffuse reflectance spectroscopy consists of determining the radiative properties of an absorbing and scattering sample from diffuse reflectance measurements. It has been applied to noninvasive health-monitoring of *in vivo* biological tissues [1–7], quality control in agricultural applications [8–12], and remote terrestrial sensing [13–16], for example. In many biological applications, the irradiated medium can be modeled as a strongly scattering multilayer medium whose radiative properties are constant within each layer but differ from layer to layer. For example, the human cervix [17], colon [18], and skin [19] have been modeled as two-layer optical systems. Skin consists of an outer layer called the epidermis and of an underlying layer called the dermis. The epidermis is characterized by strong absorption in the ultraviolet and visible part of the spectrum due to melanin. On the other hand, the blood and connective tissues are responsible for absorption and scattering in the dermis. In addition, the absorption characteristics of blood depend on the concentrations of oxyhemoglobin and deoxyhemoglobin [20].

Light transfer through turbid media, such as biological tissues, is governed by the radiative transfer equation (RTE). The latter expresses an energy balance in a unit solid angle $d\Omega$, about the direction $\hat{s}$ at location $\hat{r}$. The steady state RTE in a homogeneous, absorbing, scattering, but nonemitting, medium is expressed as [21,22]

0003-6935/09/356670-14$15.00/0

$$\hat{s}\cdot\nabla I_\lambda(\hat{r},\hat{s}) = -\mu_{a,\lambda} I_\lambda(\hat{r},\hat{s}) - \mu_{s,\lambda} I_\lambda(\hat{r},\hat{s}) + \frac{\mu_{s,\lambda}}{4\pi}\int_{4\pi} I_\lambda(\hat{r},\hat{s}_i)\Phi_\lambda(\hat{s}_i,\hat{s})\mathrm{d}\Omega_i, \quad (1)$$

where the spectral intensity at location $\hat{r}$ and in direction $\hat{s}$ is denoted by $I_\lambda(\hat{r},\hat{s})$ and expressed in $\mathrm{W/cm^2\cdot sr\cdot nm}$. The linear spectral absorption and scattering coefficients are denoted by $\mu_{a,\lambda}$ and $\mu_{s,\lambda}$, respectively, and are expressed in $\mathrm{cm^{-1}}$. The scattering phase function denoted by $\Phi_\lambda(\hat{s},\hat{s}_i)$ represents the probability that radiation propagating into the elementary solid angle $d\Omega_i$ around direction $\hat{s}_i$ will be scattered in direction $\hat{s}$. The first and second terms on the right-hand side of Eq. (1) represent the attenuation of the radiation intensity due to absorption and out-scattering, respectively. The last term corresponds to the augmentation of radiation due to in-scattering from all directions $\hat{s}_i$ into direction $\hat{s}$. The contribution of scattering to the overall extinction is represented by the single-scattering albedo ω_λ expressed as

$$\omega_\lambda = \frac{\mu_{s,\lambda}}{\mu_{a,\lambda}+\mu_{s,\lambda}}. \quad (2)$$

The Henyey–Greenstein scattering phase function is an approximate expression that accounts for the anisotropic nature of scattering and is given by [23]

$$\Phi_\lambda(\hat{s}_i,\hat{s}) = \frac{1-g_\lambda}{(1+g_\lambda^2-2g_\lambda\cos\Theta)^{3/2}}. \quad (3)$$

The Henyey–Greenstein asymmetry factor g_λ is the first moment of the scattering phase function and is defined as [23]

$$g_\lambda = \frac{1}{4\pi}\int_{4\pi}\Phi_\lambda(\hat{s}_i,\hat{s})\cos\Theta\mathrm{d}\Omega_i. \quad (4)$$

It varies between -1 and 1. If scattering is isotropic, then the phase function is constant and g_λ equals 0. For g_λ close to -1 and 1, scattering is strongly backward or forward, respectively. The Henyey–Greenstein phase function depends only on g_λ and has been used extensively in tissue optics [4,24,25], computer animation [26,27], and astronomy [28,29], to name a few.

For the sake of clarity, the dependence of the radiative properties on wavelength will be assumed and the subscript "λ" omitted henceforth. Furthermore, all analysis and results will be presented in terms of the transport single-scattering albedo ω_{tr} defined as

$$\omega_{tr} = \frac{\mu_{s,tr}}{\mu_{s,tr}+\mu_a} = \frac{\mu_s(1-g)}{\mu_s(1-g)+\mu_a}. \quad (5)$$

Here, $\mu_{s,tr} = \mu_s(1-g)$ is the transport scattering coefficient that accounts for both the magnitude and anisotropy of the scattering phenomenon [21]. For example, in the case of complete forward scattering, i.e., $g = 1.00$, scattering has no effect on the propagation of light through the medium and $\mu_{s,tr} = 0.0$ [21].

The objective of this study is to develop simple and accurate expressions for the diffuse reflectance of semi-infinite and two-layer absorbing and scattering media. Such expressions could be combined with an inverse method to retrieve the radiation properties and thickness of these media based on spectral diffuse reflectance measurements.

2. Background

Explicit analytical solutions of the RTE can be found only for a limited range of geometries and for simplified scattering phase functions [21,30]. Approximate or numerical solutions can be obtained based on the two-flux approximation or Monte Carlo simulations, for example.

A. Two-Flux Approximation

The one-dimensional (1D) RTE can be solved by the well-known two-flux approximation [31,32] (also called the Kubelka–Munk theory) in which the forward and backward fluxes are defined as

$$F^+(z) = 2\pi\int_0^{\pi/2} I(z,\theta)\cos\theta\sin\theta\mathrm{d}\theta,$$
$$F^-(z) = -2\pi\int_{\pi/2}^{\pi} I(z,\theta)\cos\theta\sin\theta\mathrm{d}\theta, \quad (6)$$

where z is the depth within the medium estimated from the front surface and θ is the angle measured from the inward normal (see Fig. 1). Then, the RTE simplifies to a set of two coupled linear equations [31,32]:

$$\frac{1}{S}\frac{dF^+}{dz} = -aF^+ + F^-, \quad (7)$$

$$\frac{1}{S}\frac{dF^-}{dz} = -F^+ + aF^-, \quad (8)$$

with $a = (S+K)/S$, where K and S are the Kubelka–Munk (K-M) absorption and scattering coefficients, respectively. They do not have any physical meaning [33], but are related to the radiative properties μ_a and $\mu_{s,tr}$ and depend on the scattering phase function.

Equations (7) and (8) have been solved for a variety of slab geometries and boundary conditions. Saunderson [34] used the two-flux approximation to predict the diffuse reflectance, denoted by $\tilde{R}_-(a)$, of a semi-infinite homogeneous medium exposed to collimated and normally incident radiation with index mismatch at the air/medium interface as [34]

$$\tilde{R}_-(a) = \rho_{01} + (1-\rho_{01})(1-\rho_{10})\frac{\tilde{R}_d(a)}{1-\rho_{10}\tilde{R}_d(a)}, \quad (9)$$

where $\tilde{R}_d(a) = a - \sqrt{a^2 - 1}$ is the diffuse reflectance of a semi-infinite medium exposed to diffuse irradiation as predicted by the two-flux approximation. Note that the first term ρ_{01} corresponds to the specular reflection of incident radiation by the surrounding/medium interface, while the second term accounts for the backscattered radiation. The specular reflectivity for normally incident radiation denoted by ρ_{01} is defined as [21]

$$\rho_{01} = \left(\frac{n_1 - n_0}{n_1 + n_0}\right)^2. \tag{10}$$

The hemispherical–hemispherical reflectivity ρ_{10} is the fraction of radiation from within the medium reflected back into the medium due to index mismatch [35] and assumed to be diffusely incident upon the medium/air interface. It is given by [34–36]

$$\rho_{10} = \int_0^{\pi/2} \rho''(\theta_i) \sin 2\theta_i \mathrm{d}\theta_i, \tag{11}$$

where $\rho''(\theta_i)$ is the directional specular reflectivity of the interface for angle of incidence θ_i expressed as [21]

$$\rho''(\theta_i) = \begin{cases} \frac{1}{2}\left[\frac{\sin^2(\theta_i - \theta_t)}{\sin^2(\theta_i + \theta_t)} + \frac{\tan^2(\theta_i - \theta_t)}{\tan^2(\theta_i + \theta_t)}\right] & \text{for } \theta_i \le \theta_c \\ 1 & \text{for } \theta_i > \theta_c \end{cases}, \tag{12}$$

where θ_t is the angle of transmittance given by Snell's law (i.e., $n_0 \sin\theta_t = n_1 \sin\theta_i$) and θ_c is the critical angle defined as $\theta_c = \sin^{-1}(n_0/n_1)$ [21].

Moreover, the diffuse reflectance of a two-layer system composed of a plane-parallel slab (Layer 1) of thickness L_1 over a semi-infinite layer (Layer 2) exposed to collimated and normally incident irradiation has been derived as [34,35]

$$\tilde{R}_{=}(a_1, a_2, Y_1) = \rho_{01} + \frac{(1-\rho_{01})(1-\rho_{10})[b_1\tilde{R}_d(a_2) + (1 - a_1\tilde{R}_d(a_2))\tanh(Y_1)]}{b_1(1 - \rho_{10}\tilde{R}_d(a_2)) + [a_1(\rho_{10}\tilde{R}_d(a_2) + 1) - {\rho_{10}}^2 - \tilde{R}_d(a_2)]\tanh(Y_1)}, \tag{13}$$

where $a_j = (S_j + K_j)/S_j$; $b_j = \sqrt{a_j^2 - 1}$, where subscript "j" refers to medium 1 or 2; and the K-M optical thickness is given by $Y_1 = b_1 S_1 L_1$.

If the medium is isotropically scattering, then $K = 2\mu_a$ and $S = \mu_{s,tr}$ [21,37]. However, when scattering is anisotropic, K and S depend on ω_{tr}. To find this relationship, the following approximate phase function can be used to reduce the RTE into a form that can be solved analytically [21,22,30,38]:

$$\Phi_\lambda(\hat{s}_i, \hat{s}) = [4g\delta(1 - \cos\Theta) + (1 - g)]. \tag{14}$$

It has the same zeroth and first moments as the Henyey–Greenstein phase function [Eq. (3)], which are equal to 1 and g, respectively. Van Gemert and Star [22] showed that the expression of the diffuse reflectance and transmittance found by solving the 1D RTE, assuming Eq. (14) has the same algebraic form as the solution developed from the two-flux approximation. Then, they developed the following relationship between the K-M absorption and scattering coefficients K and S on the one hand and μ_a and $\mu_{s,tr}$ on the other:

$$\mu_a = \eta K, \qquad \mu_{s,\mathrm{tr}} = \chi S, \tag{15}$$

where

$$\eta = (\phi - 1)(1 - \omega_{\mathrm{tr}})/\zeta(\phi + 1),$$
$$\chi = -\omega_{\mathrm{tr}}(\phi - \phi^{-1})/(2\zeta). \tag{16}$$

The parameter ϕ is given by [22]

$$\phi = \frac{\zeta + \ln(1 - \zeta)}{\zeta - \ln(1 + \zeta)}, \tag{17}$$

where ζ is the root of the characteristic equation [30]

$$\omega_{tr} = \frac{2\zeta}{\ln[(1 + \zeta)/(1 - \zeta)]}. \tag{18}$$

To simplify the estimation of the diffuse reflectance, we solved Eq. (18) numerically and fitted a third-order polynomial to yield

$$\zeta^2 = \frac{47}{52} + \frac{31}{49}\omega_{tr} - \frac{49}{54}\omega_{tr}^2 - \frac{17}{27}\omega_{tr}^3. \tag{19}$$

The relative difference between Eq. (19) and the exact solution of Eq. (18) was found to be less than 1% for $0.40 < \omega_{\mathrm{tr}} < 1.00$. Finally, the K-M optical thickness is given by

$$Y_1 = \zeta(\mu_a + \mu_{s,tr})L_1 = \zeta\tau_{tr,1}, \tag{20}$$

where $\tau_{tr,1} = (\mu_a + \mu_{s,tr})L_1$ is the transport optical thickness of a slab of thickness L_1 [21].

B. Monte Carlo Methods

Alternatively, Monte Carlo methods are commonly used to numerically solve the RTE [39–43]. To do so, a stochastic model is constructed such that the expected value of a certain random variable is equivalent to the value of a physical quantity that is determined by the exact differential equation [44]. The expected value is estimated by sampling the random variable multiple times. In effect, by repeating the simulation, the variance of the estimate diminishes. Thus, the solution may be found with arbitrary accuracy by increasing the number of simulations, albeit at the cost of time [45].

Therefore, Monte Carlo simulations are difficult to use in inverse methods associated with diffuse reflectance spectroscopy [21]. Indeed, the forward problem of evaluating the diffuse reflectance must be solved numerous times to iteratively determine the medium's radiative properties. Instead, Gardner *et al.* [41] developed a semiempirical model for 1D light transfer through a semi-infinite medium exposed to collimated incident radiation based on Monte Carlo simulations. An analytical model of the fluence profile in the medium was developed using the diffusion approximation. The constants of integration, instead of being determined analytically, were found by fitting them to results from Monte Carlo simulations. The predictions of local fluence by the semiempirical model compared well with results from Monte Carlo simulations and could be rapidly estimated.

The objective of this study is to develop a semiempirical model for the diffuse reflectance of a nonemitting, absorbing, and strongly forward-scattering medium consisting of two layers exposed to collimated incident radiation. An approach similar to that used by Gardner *et al.* [41], but based on the two-flux approximation, is developed in this study.

3. Methods

A. Model Geometry and Radiative Properties

Figure 1 shows the 1D geometries investigated in this study. First, a homogeneous semi-infinite slab characterized by μ_a, μ_s, g, and n_1 was considered. A wide range of property values was explored, namely, $0.3 \le \omega_{\mathrm{tr}} \le 0.99$, $0.70 \le g \le 0.90$, and $n_1 = 1.00$, 1.33, 1.44, 1.77, and 2.00.

Moreover, a two-layer medium was considered. It consisted of a plane-parallel slab (Layer 1) characterized by $\mu_{a,1}$, $\mu_{s,tr,1}$, g_1, n_1, and thickness L_1, supported by a semi-infinite sublayer (Layer 2) characterized by $\mu_{a,2}$, $\mu_{s,tr,2}$, and g_2. The polar angle θ is taken relative to the inward surface normal. The physical distance from the surface is denoted by z and measured in centimeters. The thickness of Layer 1, denoted by L_1, was considered between 0 and infinity. The incident light source was modeled as a collimated, monochromatic, and normally incident beam of infinite radius and intensity $I_0 = q_0\delta(\theta)$. The quantity q_0 denotes the radiative flux of the collimated beam and $\delta(\theta)$ is the Dirac delta function. The air/slab interface and the interface between the slab and the semi-infinite sublayer are assumed to be optically smooth. Under these conditions, radiative transfer can be considered as 1D [21,46]. Light scattering was assumed to dominate over absorption in both layers and to be strongly forward. The transport single-scattering albedo of the slab $\omega_{tr,1}$ and of the sublayer $\omega_{tr,2}$ varied between 0.50 and 0.99. The Henyey–Greenstein asymmetry factors of the two layers, g_1 and g_2, varied between 0.70 and 0.90. These ranges correspond, but are not limited to, biological tissues, such as skin, muscle, and brain [4]. Finally, the index of refraction was assumed to be identical within the two layers but different from that of the surroundings. The values of refractive index investigated were $n_1 = n_2 = 1.00$, 1.33, and 1.44, corresponding to vacuum, water in the visible [47], and biological tissues in the visible and near-infrared part of the electromagnetic spectrum [4,24]. The surrounding was assumed to be air or vacuum, so that $n_0 = 1.00$.

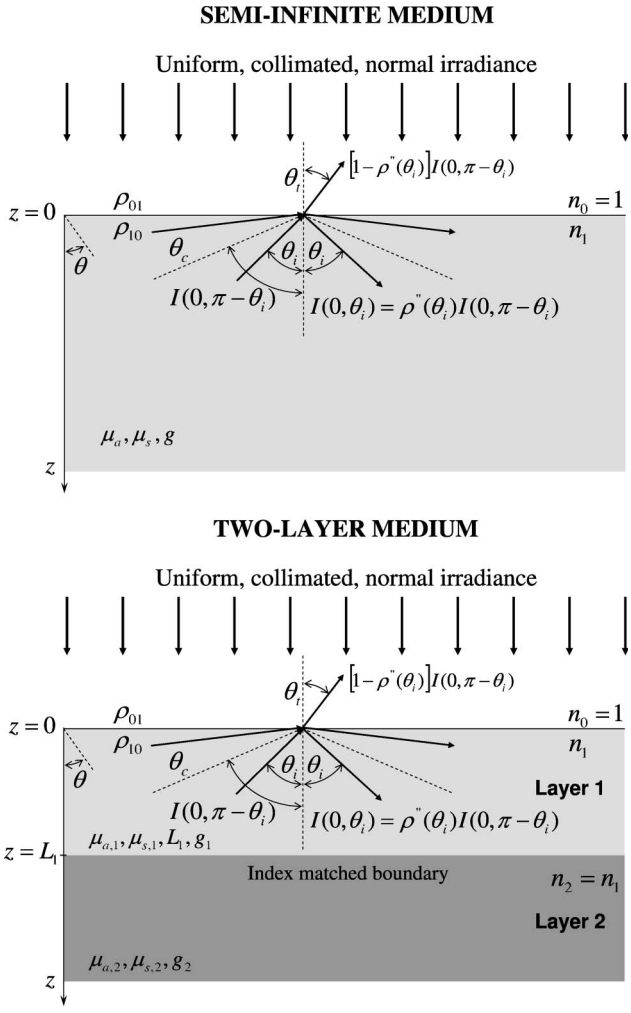

Fig. 1. Schematic of the semi-infinite and two-layer media considered along with coordinate system and boundary conditions.

The RTE given in Eq. (1) was solved numerically for both geometries after specifying the boundary conditions and selecting the method of solution.

B. Boundary Conditions

Because of index mismatch, the collimated intensity incident onto the air/slab interface is reflected and refracted according to Fresnel's equations and Snell's law, respectively. The flux transmitted through the air/slab interface is $(1-\rho_{01})q_0$, while the reflected flux is $\rho_{01}q_0$. In addition, light from within the slab and incident onto the slab/air interface at an oblique angle θ_i is specularly reflected with intensity $\rho''(\theta_i)I(0,\pi-\theta_i)$. On the other hand, light backscattered from within the medium that is incident on the slab/air interface at an angle θ_i larger than the critical angle undergoes total internal reflection, as illustrated in Fig. 1. Therefore, the boundary conditions of the RTE at the slab/air interface ($z=0$) can be expressed as [21]

$$I(0,\theta) = (1-\rho_{01})q_0\delta(\theta) + \rho''(\theta)I(0,\pi-\theta) \quad \text{for } 0 \le \theta \le \pi/2. \tag{21}$$

Furthermore, the intensity vanishes as z tends to infinity, i.e.,

$$I(z\to\infty,\theta) = 0 \quad \text{for } -\pi \le \theta \le \pi. \tag{22}$$

Note that no reflection or refraction takes place at the slab/sublayer interface since they have the same index of refraction. Thus, no boundary conditions need be imposed.

C. Method of Solution

The RTE was solved using the Monte Carlo simulation software developed by Wang and Jacques [48] for simulating light transfer through multilayer nonemitting, absorbing, and scattering media. The Henyey–Greenstein scattering phase function, given by Eq. (3), was used to account for anisotropic scattering. A complete and detailed description of the implementation and theoretical underpinnings of this software is given in Ref. [48]. The variance in the prediction of the diffuse reflectance increases with decreasing single-scattering albedo since absorption by the medium dominated over scattering, resulting in fewer backscattered photons. Thus, the number of simulated photon packets per simulation was increased until the variance associated with the estimate of the diffuse reflectance fell below 1% for the most stringent case of a homogeneous medium with $\omega_{tr}=0.50$. Each simulation required 1,000,000 photon packets or less to achieve the convergence criteria.

D. Diffuse Reflectance

The total intensity of the light reflected from semi-infinite or two-layer media is the sum of the specularly reflected intensity and the intensity backscattered by the medium and transmitted through the slab/air interface. In practice, this quantity can be measured *in vivo* by a variety of optical instruments, such as an integrating sphere coupled to a detector [4]. It is denoted by $I_r(\theta_t)$ and expressed as

$$I_r(\theta_t) = \rho_{01}q_0\delta(\pi-\theta_t) + [1-\rho''(\theta_i)]I(0,\pi-\theta_i) \quad \text{for } 0 \le \theta_i \le \pi/2, \tag{23}$$

where θ_i is given by Snell's law. The specularly reflected intensity $\rho_{01}q_0\delta(\pi-\theta_t)$ was ignored in this study. In practice, this is achieved by illuminating the medium with polarized light [49]. The specularly reflected intensity remains polarized and can be filtered by a linear polarizer before reaching the detector [49]. The backscattered light is depolarized due to multiple scattering in the medium and passes unattenuated through the polarizer filter to reach the detector. Thus, the diffuse reflectance R is defined as the ratio of the backscattered radiative flux q_r to the incident radiative flux, q_0, i.e., $R=q_r/q_0$, where q_r is expressed as

$$q_r = -2\pi\int_{\pi/2}^{\pi}[1-\rho''(\theta_t)]I(0,\pi-\theta_t)\cos\theta_t\sin\theta_t d\theta_t. \tag{24}$$

The goal of the study is to develop an expression to rapidly predict the diffuse reflectance of a two-layer medium as a function of its radiative and geometrical properties, namely, $n_1=n_2$, L_1, $\mu_{a,1}$, $\mu_{s,1}$, $\mu_{a,2}$, $\mu_{s,2}$, g_1, and g_2. As an intermediate step, an expression for the reflectance of a semi-infinite medium is developed.

4. Analysis

A. Semiempirical Diffuse Reflectance of Semi-Infinite Media

This section aims to determine the relationship between the diffuse reflectance R_- from a semi-infinite layer and its transport single-scattering albedo ω_{tr} with higher accuracy than the original two-flux approximation. Prediction accuracy was calculated relative to results from Monte Carlo simulations. Figure 2 shows the diffuse reflectance R_- as a function of ω_{tr} for $n_1=1.00$ for different values of g, along with the predictions from the two-flux approximation given by Eq. (9) and values of a obtained from Eqs. (15)–(17) and (19). It is evident that the diffuse reflectance R_- increases with ω_{tr} as scattering dominates over absorption and more light is backscattered by the medium. Furthermore, the diffuse reflectance is almost completely determined by ω_{tr} and is nearly independent of the Henyey–Greenstein asymmetry factor g in the range of interest. This is known as the similarity relation [38].

Moreover, the reflectance predicted by the two-flux approximation follows a similar trend as that predicted by Monte Carlo simulations (Fig. 2). However, the relative difference varies from 100% to 5% as ω_{tr} increases from 0.3 to 1.0 for all values of g considered. This can be attributed to the fact that Eq. (11), used

to determine ρ_{10}, was derived with the assumption that intensity at the medium/air interface was diffuse [34,35]. It has been shown that this is not the case [50]. Thus, unlike Monte Carlo simulations, ρ_{10} used in the two-flux approximation does not accurately account for the optical phenomena at the medium/air interface.

Consequently, Eq. (9), predicting the reflectance of a semi-infinite medium, was replaced by the following semiempirical expression:

$$R_{-}(\omega_{tr}) = [1-\rho_{01}][1-\hat{\rho}_{10}(\omega_{tr})]\frac{\hat{R}_d(\omega_{tr})}{1-\hat{\rho}_{10}(\omega_{tr})\hat{R}_d(\omega_{tr})}, \tag{25}$$

where ρ_{01} is given by Eq. (10). To account for the fact that intensity $I(z=0,-1\le\mu\le 0)$ inside the medium is not diffuse, the reflectivity ρ_{10} and the reflectance $\tilde{R}_d$ in Eq. (9) were replaced by $\hat{\rho}_{10}$ and $\hat{R}_d$, respectively, which are assumed to be polynomial functions of $a(\omega_{tr})$:

$$\hat{\rho}_{10}(\omega_{tr}) = \rho_{10} + \sum_{i=0}^{i=N} A_i[a(\omega_{tr})]^i, \tag{26}$$

$$\hat{R}_d(\omega_{tr}) = \tilde{R}_d(a(\omega_{tr})) + \sum_{i=0}^{i=N} B_i[a(\omega_{tr})]^i, \tag{27}$$

where $(A_i)_{0\le i\le N}$ and $(B_i)_{0\le i\le N}$ are regression coefficients and N is the polynomial order. These parameters were found by minimizing the sum of the squared residuals between the reflectance R_{-} obtained by Monte Carlo simulations and that predicted by Eqs. (25)–(27). Numerical results were found for $n_1 = 1.00$, 1.33, 1.44, 1.77, and 2.00. The polynomial order N was increased until the residual between the diffuse reflectance determined by Monte Carlo simulations and Eq. (25) was small and random. This condition was met with $N=3$. More precisely, for $0.70\le g\le 0.90$, the residual was less than (i) 10% for $\omega_{tr}\ge 0.40$, (ii) 5% for $\omega_{tr}\ge 0.50$, and (iii) 2% for $\omega_{tr}\ge 0.70$.

Figure 3 shows the diffuse reflectance from a semi-infinite medium as a function of its transport single-scattering albedo ω_{tr} for different values of n_1 and g. Predictions by Eqs. (25)–(27) are also plotted for the regression coefficients $(A_i)_{0\le i\le 3}$ and $(B_i)_{0\le i\le 3}$ as reported in Table 1. The similarity relationship previously observed for the case of $n_1 = 1.00$ (Fig. 2) was also valid for other values of n_1. Thus, the diffuse reflectance of a semi-infinite medium R_{-} is only a function of (i) the index of refraction n_1 and (ii) the transport single-scattering albedo ω_{tr}.

B. Diffuse Reflectance of Two-Layer Media—Two-Flux Approximation

Figure 4(a) shows the diffuse reflectance of the two-layer medium $\tilde{R}_{=}(a_1,a_2,Y_1)$ predicted by Eq. (13) as a function of the K-M optical thickness Y_1 for nine

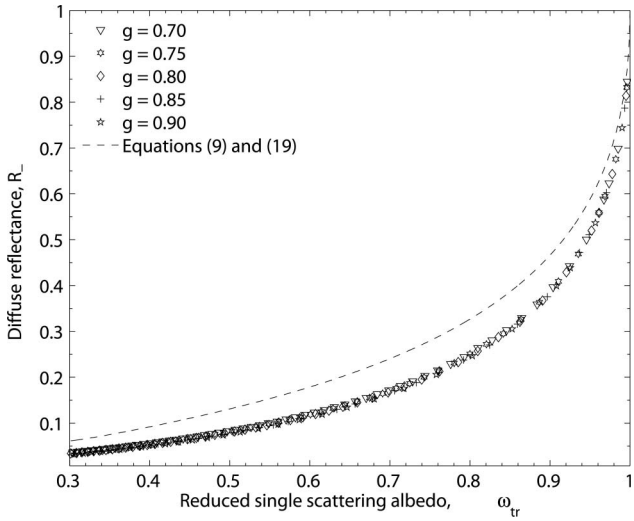

Fig. 2. Diffuse reflectance of a homogeneous semi-infinite medium predicted by Monte Carlo simulations (symbols) and the two-flux approximation [Eqs. (9) and (19)] (dashed curve) for $n_1 = 1.00$, $0.3\le\omega_{tr}\le 1.00$, and $0.70\le g\le 0.90$.

pairs of parameters a_1 and a_2 varying between 1 and 6, while $\rho_{01} = 0.033$ and $\rho_{10} = 0.56$. These values correspond to $\omega_{tr,1}$ and $\omega_{tr,2}$ varying between 0.50 and 1.00, $n_0 = 1.00$, and $n_1 = n_2 = 1.44$. Figure 4(a) shows that the diffuse reflectance of the two-layer medium progresses from $\tilde{R}_{-}(a_2)$ to $\tilde{R}_{-}(a_1)$ as Y_1 increases from 10^{-3} to 6. Indeed, there are two asymptotic cases:

$$\begin{aligned}\tilde{R}_{=}(a_1,a_2,Y_1) &\underset{Y_1\to 0}{\to} \tilde{R}_{-}(a_2),\\ \tilde{R}_{=}(a_1,a_2,Y_1) &\underset{Y_1\to\infty}{\to} \tilde{R}_{-}(a_1),\end{aligned} \tag{28}$$

where $\tilde{R}_{-}(a)$ is given by Eq. (9) and shown in Fig. 4(a). In other words, the two-layer medium behaves as a semi-infinite medium as the top layer becomes either

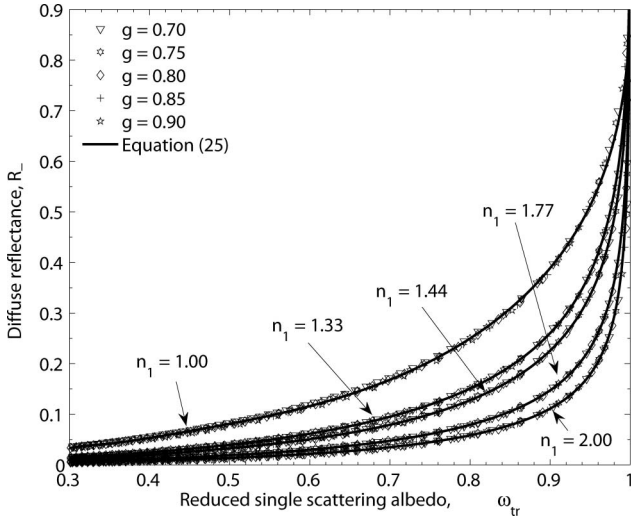

Fig. 3. Diffuse reflectance of a semi-infinite homogeneous medium predicted by Monte Carlo simulations and Eqs. (25) for $n_1 = 1.00$, 1.33, 1.44, 1.77, and 2.00, $0.3\le\omega_{tr}\le 1.0$, and $0.7\le g\le 0.9$.

Table 1. Regression Coefficients $(A_i)_{0\le i\le 3}$ and $(B_i)_{0\le i\le 3}$ Used in Eqs. (26) and (27) to Estimate the Diffuse Reflectance R_- of a Semi-Infinite Homogeneous Medium with Index of Refraction $n_1 = 1.33$, 1.44, 1.77, and 2.00

n_1	$i=$	0	1	2	3
1.00	$A_i=$	0	0	0	0
	$B_i=$	-6.387×10^{-2}	-1.282×10^{-2}	5.701×10^{-3}	-4.503×10^{-4}
1.33	$A_i=$	-6.738×10^{-1}	1.767	−1.554	5.855×10^{-1}
	$B_i=$	-9.898×10^{-2}	6.117×10^{-3}	3.774×10^{-1}	-6.291×10^{-1}
1.44	$A_i=$	-6.696×10^{-1}	1.853	−1.732	6.791×10^{-1}
	$B_i=$	-1.189×10^{-1}	7.524×10^{-3}	5.606×10^{-1}	-9.807×10^{-1}
1.77	$A_i=$	-6.322×10^{-1}	1.716	−1.625	6.574×10^{-1}
	$B_i=$	-1.192×10^{-1}	7.863×10^{-3}	7.001×10^{-1}	−1.254
2.00	$A_i=$	-4.688×10^{-1}	1.234	−1.139	4.544×10^{-1}
	$B_i=$	-8.223×10^{-2}	5.441×10^{-3}	6.325×10^{-1}	−1.123

optically thin or thick. This behavior suggests the definition of a reduced reflectance as

$$\tilde{R}^* = \frac{\tilde{R}_=(a_1,a_2,Y_1) - \tilde{R}_-(a_2)}{\tilde{R}_-(a_1) - \tilde{R}_-(a_2)}, \tag{29}$$

where $\tilde{R}^*$ increases from 0 to 1 as Y_1 varies from 0 to infinity. After combining Eqs. (13) and (29), the reduced reflectance can be expressed as a function of two dimensionless parameters, $\tilde{\alpha}$ and Y_1,

$$\tilde{R}^*(\tilde{\alpha},Y_1) = \frac{\tanh(Y_1)}{1/\tilde{\alpha} + (1-1/\tilde{\alpha})\tanh(Y_1)}, \tag{30}$$

where $\tilde{\alpha}$ is given by

$$\tilde{\alpha} = 1 + \frac{\rho_{10} + \tilde{R}_d(a_2)a_1[\rho_{10}\tilde{R}_d(a_2)+1]}{\sqrt{a_1^2-1}[\rho_{10}\tilde{R}_d(a_2)-1]}. \tag{31}$$

Figure 4(b) shows $\tilde{R}^*$ as a function of Y_1 for the same values of a_1 and a_2 used to produce Fig. 4(a). Unlike $\tilde{R}_=$ shown in Fig. 4(a), $\tilde{R}^*$ is nearly independent of a_1 and a_2. Furthermore, $\tilde{\alpha}$ was found to be nearly constant and equal to 2.0 for a_1 and a_2 between 1.0 and 6.0, or for $\omega_{tr,1}$ and $\omega_{tr,2}$ between 0.50 and 0.99. Similar results were obtained for other values of $n_1 = n_2$ between 1.00 and 2.00.

C. Diffuse Reflectance of a Two-Layer System—Semiempirical Expression

A semiempirical approach similar to that presented in Subsection 4.A for a semi-infinite medium was applied to the two-layer medium described in Fig. 1 to improve the accuracy of the two-flux approximation in predicting the diffuse reflectance of two-layer media. Results from Monte Carlo simulations presented in this section correspond to the case where $g_1 = g_2$. However, similar results hold for a given pair of $\omega_{tr,1}$ and $\omega_{tr,2}$ when g_1 and g_2 are different, and regardless of their values between 0.7 and 0.9. This will be shown numerically in Subsection 5.A.

Figures 5(a) and 5(c) show the diffuse reflectance $R_=$ of a two-layer system determined by Monte Carlo simulations as a function of Y_1 for $\omega_{tr,2} = 0.479$ and $\omega_{tr,2} = 0.958$, with $g_1 = g_2 = 0.77$, $n_1 = n_2 = 1.44$, and $\omega_{tr,1}$ ranging between 0.50 and 0.99. The asymp-

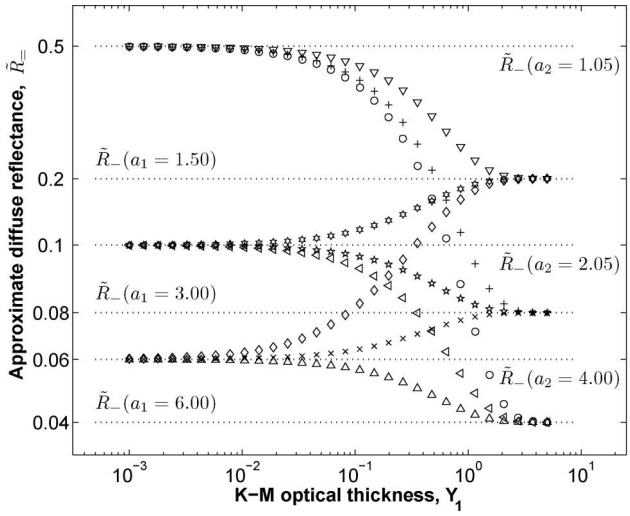

(a)

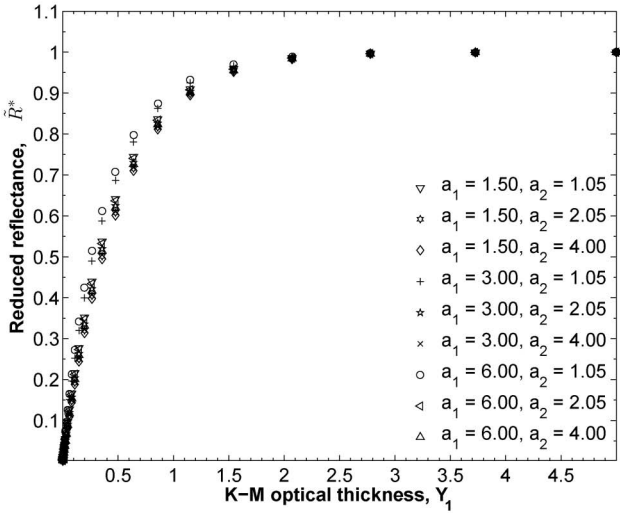

(b)

Fig. 4. (a) Diffuse reflectance of two-layer optical medium $\tilde{R}_=(a_1,a_2,Y_1)$ as a function of Y_1 predicted by Eq. (13). Asymptotic values of $R_-(a)$ were computed from Eq. (9). (b) Reduced diffuse reflectance $\tilde{R}^*$ given by Eq. (29) as a function of Y_1 for different values of a_1 and a_2; $\rho_{01} = 0.033$ and $\rho_{10} = 0.56$. The legend applies to both figures.

totic values for smaller and larger values of Y_1 were calculated using Eqs. (25)–(27). The slope of $R_=(Y_1)$ was found to be positive for $\omega_{tr,1} > \omega_{tr,2}$ and negative otherwise. Furthermore, the slope of $R_=(Y_1)$ with respect to Y_1 increases as the difference between $\omega_{tr,1}$ and $\omega_{tr,2}$ increases.

Here, also, a reduced reflectance R^* can be defined by analogy with $\tilde{R}^*$ given by Eq. (29):

$$R^* = \frac{R_= - R_-(\omega_{tr,2})}{R_-(\omega_{tr,1}) - R_-(\omega_{tr,2})}. \tag{32}$$

Note that the predictions of the single-layer diffuse reflectance by the two-flux approximation $\tilde{R}_-(a_1)$ and $\tilde{R}_-(a_2)$ are replaced by the more accurate $R_-(\omega_{tr,1})$ and $R_-(\omega_{tr,2})$ predicted by Eq. (25). Figures 5(b) and 5(d) show the reduced reflectance R^* as a function of Y_1 for the same parameters used to produce Figs. 5(a) and 5(c), respectively. It establishes that R^* collapses onto a single curve for $\omega_{tr,1}$ ranging between 0.50 and 0.99. In fact, no value of R^* deviates from the mean value of R^* by more than 10% for all $\omega_{tr,1}$.

The evolution of R^* differs significantly from $\tilde{R}^*$ predicted by the two-flux approximation and given by Eqs. (30) and (31). However, Eq. (30) can be used if the parameter $\tilde{\alpha}$ is replaced by an empirical parameter α, i.e.,

$$R^* = \frac{\tanh(Y_1)}{1/\alpha + (1 - 1/\alpha)\tanh(Y_1)}, \tag{33}$$

where α was found by least-squares fitting of Monte Carlo simulations for R^*. A single value of α was sufficient to fit the results from Monte Carlo simulations for given values of n_1 and $\omega_{tr,2}$ and different values of $\omega_{tr,1}$ and g, i.e., $\alpha = \alpha(n_1, \omega_{tr,2})$. Predictions of the reduced reflectance R^* as a function of Y_1 by Eq. (33) using $\alpha = 1.104$ are in close agreement with the more

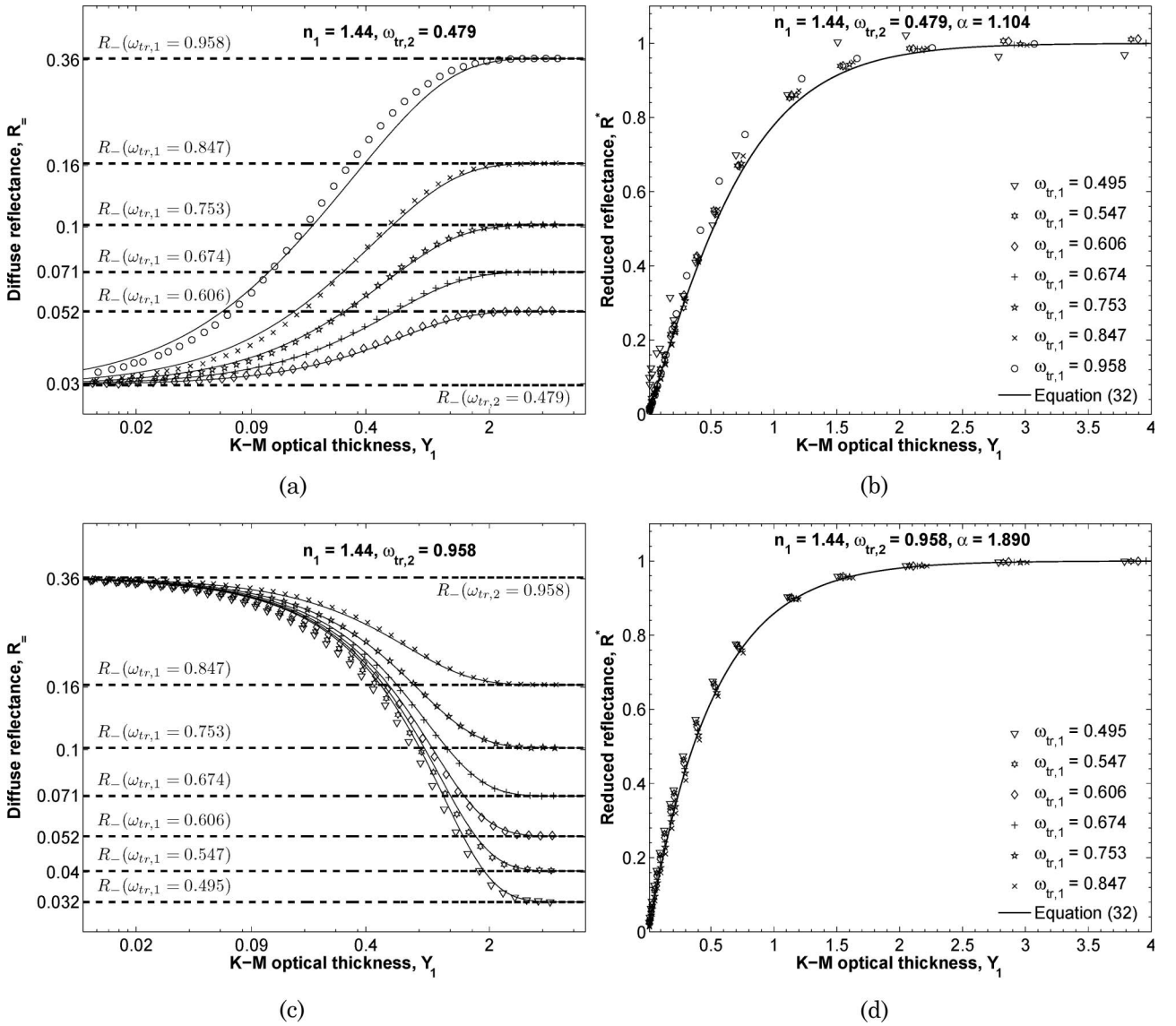

Fig. 5. Diffuse reflectance $R_=$ predicted by Monte Carlo simulations as a function of Y_1 and corresponding reduced reflectance R^* [Eq. (32)] for $n_1 = 1.44$ and (a), (b) $\omega_{tr,2} = 0.479$ and (c), (d) $\omega_{tr,2} = 0.958$. Predictions of $R_=$ by Eqs. (33) and (34) are also shown (solid curve).

accurate Monte Carlo simulations. Thus, the diffuse reflectance of a two-layer medium can be expressed as

$$R_{=} = R^{*}[R_{-}(n_1, \omega_{tr,1}) - R_{-}(n_1, \omega_{tr,2})] + R_{-}(n_1, \omega_{tr,2}), \tag{34}$$

where R_{-} and R^{*} are given by Eqs. (25) and (33), respectively. The reconstruction of the diffuse reflectance $R_{=}$ from Eq. (34) agrees well with predictions from Monte Carlo simulations. The primary source of disagreement lies in the 2% to 5% relative error in $R_{-}(\omega_{tr,1})$ and $R_{-}(\omega_{tr,2})$ between Monte Carlo simulations and predictions by Eqs. (25)–(27) for $\omega_{tr} \leq 0.70$. For example, in Fig. 5(a), for $\omega_{tr,1} = 0.479$, the reduced diffuse reflectance predicted by Eq. (33) deviates from Monte Carlo simulations by up to 6%. On the other hand, for $\omega_{tr,1} = 0.958$, the predictions do not deviate by more than 2%.

The above analysis was repeated for $0.50 \leq \omega_{tr,1} \leq 0.99$, $0.70 \leq g_1 = g_2 \leq 0.90$, and $0.50 \leq \omega_{tr,2} \leq 0.99$ for different values of $n_1 = n_2$. Figure 6(a) shows the parameter $1/\alpha$ found for $n_1 = 1.44$ and $0.70 \leq g_1 = g_2 \leq 0.90$ as a function of $\omega_{tr,2}$. It is apparent that $1/\alpha$ varies slightly with $g_1 = g_2$ and $\omega_{tr,1}$ for a given $\omega_{tr,2}$. Figure 6(b) shows $1/\alpha$ as a function of $\omega_{tr,2}$ for $n_1 = 1.00$, 1.33, and 1.44, and $0.70 \leq g_1 = g_2 \leq 0.90$. Also shown are the following approximate polynomial expressions for $1/\alpha$ given by

$$1/\alpha = C(n_1)\omega_{tr,2}^2 + D(n_1)\omega_{tr,2} + E(n_1), \tag{35}$$

where C, D, and E depend on n_1 and are given in Table 2 for $n_1 = 1.00$, 1.33, and 1.44.

Unlike a polynomial or other series expansion, expressing R^{*} by Eq. (33) is well behaved in and outside the pertinent range of Y_1. It is attractive, also, because it can be estimated using the single semiempirical parameter α. In other words, the diffuse reflectance of a two-layer medium, which, *a priori*, depends on eight parameters ($\mu_{a,1}$, $\mu_{s,1}$, L_1, $\mu_{a,2}$, $\mu_{s,2}$, g_1, g_2, and $n_1 = n_2$) was reduced to a function of only three dimensionless parameters, namely, Y_1, $\omega_{tr,1}$, and α. The parameter $\alpha(n_1, \omega_{tr,2})$ provides intuitive insight into the effects of the top layer on the diffuse reflectance of the two-layer medium. Differentiating Eq. (33) with respect to Y_1 and setting $Y_1 = 0$ yields α, i.e.,

$$\frac{\partial R^{*}}{\partial Y_1}(Y_1 = 0, \omega_{tr,1}, \omega_{tr,2}) = \alpha.$$

In other words, α is a measure of how effectively the top layer optically "shields" the semi-infinite layer. For larger α, $R_{=}$ quickly progresses from $R_{-}(\omega_{tr,1})$ and $R_{-}(\omega_{tr,2})$.

For a given $\omega_{tr,2}$, $1/\alpha$ varies with $g_1 = g_2$ up to 7% about the quadratic fits. However, the reduced diffuse reflectance R^{*} was found to be relatively insensitive to these variations. In fact, for the index matched case ($n_1 = n_0$), $1/\alpha$ can be treated as a constant equal to $1/\alpha = 0.656$. This increases the relative error in the prediction of $R_{=}$ by Eq. (34), but never by more than 0.1%.

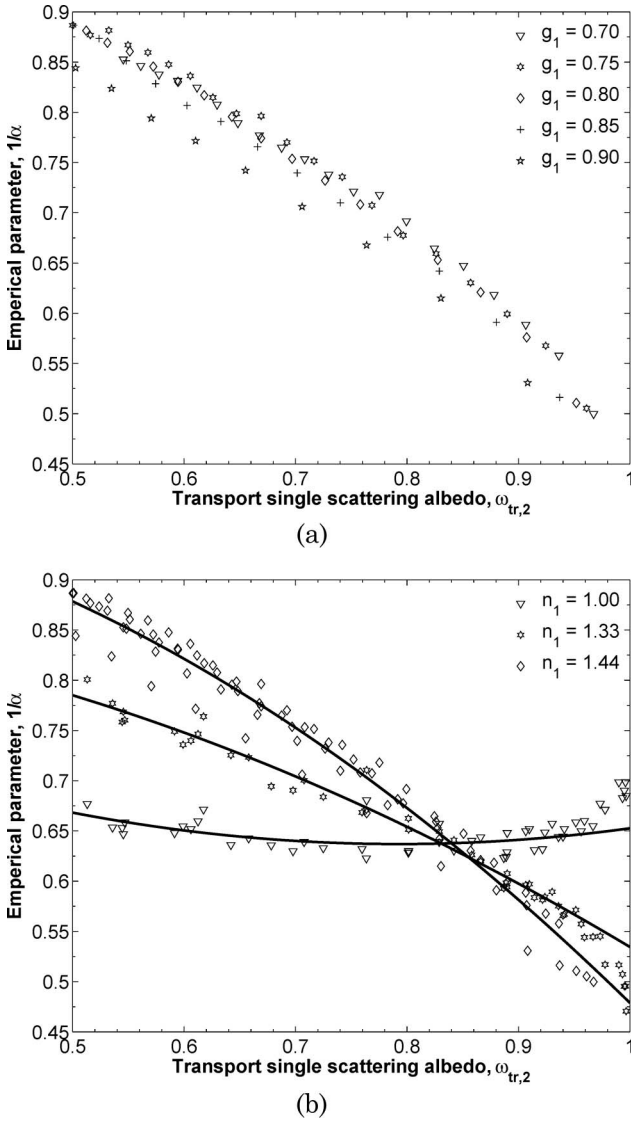

Fig. 6. (a) Relationship between $\omega_{tr,2}$ and $1/\alpha$ determined for $n_1 = n_2 = 1.44$ and $0.70 \leq g_1 = g_2 \leq 0.90$. (b) Relationship between $\omega_{tr,2}$ and $1/\alpha$ [Eq. (35) and Table 2] for $n_1 = n_2 = 1.00$, 1.33, and 1.44, and $0.70 \leq g_1 = g_2 \leq 0.90$.

5. Results and Discussion

A. Comparison of Model Predictions with Monte Carlo Simulations

The accuracy of Eqs. (33)–(35) with values of C, D, and E from Table 2 was assessed numerically for $10^{-2} \leq Y_1 \leq 6$, $0.50 \leq \omega_{tr,1} \leq 0.99$, and $0.50 \leq \omega_{tr,2} \leq 0.99$, $0.70 \leq g_1 \leq 0.90$, $0.70 \leq g_2 \leq 0.90$, and

Table 2. Regression Coefficients in the Expression of $1/\alpha$ Given by Eq. (35)

n_1	C	D	E
1.00	0.529	−0.759	0.831
1.33	−0.324	−0.016	0.874
1.44	−0.569	−0.055	0.993

$n_1 = 1.00$, 1.33 and 1.44, for values different from those used to generate the semiempirical model. For Y_1 outside of the said range, the two-layer model [Eqs. (25), (33), and (35)] can be replaced by the single-layer model [Eq. (25)]. For comparison, an additional 10,000 Monte Carlo simulations of light transfer through the two-layer medium were performed.

Figure 7(a) illustrates the relative error between predictions by Eq. (34) and results from Monte Carlo simulations as a function of the diffuse reflectance $R_=$ for $n_1 = 1.44$, $\omega_{tr,1} \geq 0.50$, $\omega_{tr,2} \geq 0.50$, and $Y_1 \geq 0$. Similar results were obtained for different values of n_1. The relative error ranged from −15% to 17%. It is evident that, as the absolute value of $R_=$ decreases, the maximum relative error increases. Figure 7(b) shows the frequency of the relative error for $n_1 = 1.00$, 1.33, and 1.44. It is established that the relative error is similar for each index of refraction

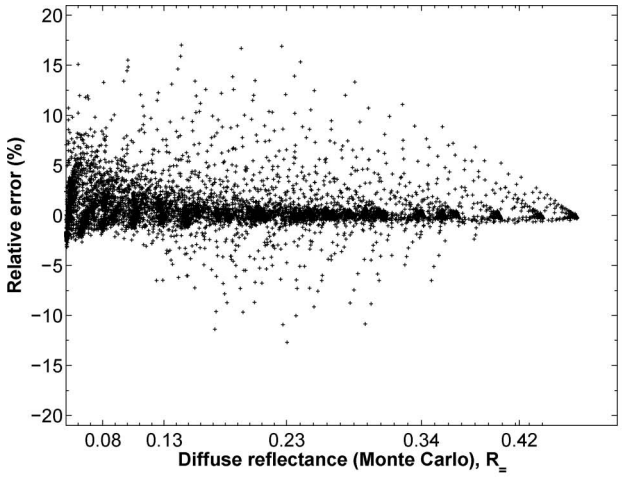

(a)

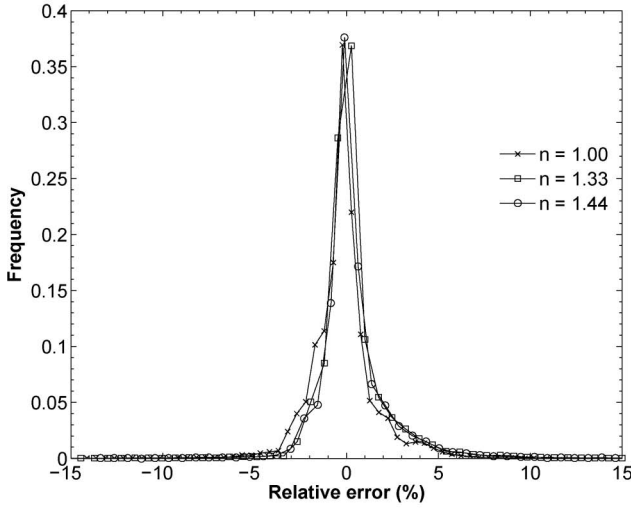

(b)

Fig. 7. (a) Relative error between predictions by Eq. (34) and Monte Carlo simulations for $n_1 = n_2 = 1.44$. (b) Histogram of the relative error for 10,000 simulations for $n_1 = n_2 = 1.00$, 1.33, and 1.44.

and is less than 20%. Quantitatively, the mean and standard deviation of the relative error averaged over all n_1 are −0.16 and 1.72%, respectively. While the method performs well on average, the relative error can be larger than 10%. This is caused by two factors: (i) the inaccuracy of $1/\alpha$ [Eq. (35)] in describing the two-layer system and (ii) the inaccuracy of Eq. (25) in predicting $R_-(\omega_{tr})$. It was determined that the effects of the latter dominate over the former and that larger relative error occurs for small $\omega_{tr,1}$ and $\omega_{tr,2}$. The accuracy of Eq. (25) in predicting $R_-(\omega_{tr})$ decreases for decreasing ω_{tr}. This, in turn, increases the relative error in Eq. (34) since $R_=$ is a function of R_-. In fact, the maximum relative error of $R_=$ predicted by Eq. (34) compared with Monte Carlo simulations was less than (i) 17% for $0.50 < \omega_{tr,1}$ and $0.50 < \omega_{tr,2}$, (ii) 10% for $0.60 < \omega_{tr,1}$ and $\omega_{tr,2} \geq 0.60$, (iii) 4.5% for $\omega_{tr,1}$ and $\omega_{tr,2} \geq 0.75$, and (iv) 1.5% for $\omega_{tr,1}$ and $\omega_{tr,2} \geq 0.85$.

B. Reflectance of Human Skin

This section focuses on diffuse reflectance spectroscopy of human skin as a way to demonstrate the usefulness and accuracy of the developed model. Optical properties of skin reported in the literature are summarized before predicting the spectral diffuse reflectance between 490 and 650 nm. For these wavelengths, the epidermis and the dermis have large and significantly different absorption coefficients, so that human skin behaves optically as a two-layer medium. In contrast, the epidermis is essentially transparent in the near-infrared and the scattering albedo approaches unity [51]. Then, the present semiempirical model is no longer valid.

The optical properties of the human skin in the visible range depend on various biological factors and can be found in the literature [4]. The epidermis is composed mainly of dead cells, keratinocytes, melanocytes, and langerhans [40]. Melanocytes synthesize melanin, the skin protein that dominates light absorption in the epidermis (Layer 1). The absorption coefficient of the epidermis $\mu_{a,1}(\lambda)$ can be expressed as [52]

$$\mu_{a,1}(\lambda) = \mu_{a,mel} f_{mel} + (1 - f_{mel})\mu_{a,back}, \qquad (36)$$

where f_{mel} is the volume fraction of melanocytes in the epidermis and $\mu_{a,back}(\lambda)$ is the background absorption of human flesh given by [52,53]

$$\mu_{a,back}(\lambda) = 7.84 \times 10^8 \lambda^{-3.255}. \qquad (37)$$

Furthermore, the absorption coefficient of a single melanocyte as a function of wavelength has been approximated as [54]

$$\mu_{a,mel}(\lambda) = 6.60 \times 10^{11} \lambda^{-3.33}. \qquad (38)$$

Here λ is expressed in nanometers and $\mu_{a,back}(\lambda)$ and $\mu_{a,mel}(\lambda)$ are in cm^{-1}.

The absorption coefficient of the dermis (Layer 2) is determined primarily by the absorption of blood [55,56] and can be written as [51,57]

$$\mu_{a,2}(\lambda) = f_{blood}\mu_{a,blood}(\lambda) + (1 - f_{blood})\mu_{a,back}(\lambda), \quad (39)$$

where f_{blood} is the volume fraction of the dermis occupied by blood. Visible light absorption by blood is dominated by the presence of oxyhemoglobin and deoxyhemoglobin so that $\mu_{a,blood} = \mu_{a,oxy} + \mu_{a,deoxy}$. The absorption coefficient of oxyhemoglobin is given by [51,57]

$$\mu_{a,oxy}(\lambda) = \epsilon_{oxy}(\lambda) C_{heme} SO_2 / 66,500, \quad (40)$$

where ϵ_{oxy} is the molar extinction coefficient of oxyhemoglobin [in $\mathrm{cm}^{-1}/(\mathrm{mole/liter})$] with molecular weight of 66,500 g/mol, C_{heme} is the concentration ratio of hemoglobin in blood [gram/liter], and SO_2 is the oxygen saturation defined as the mass ratio of oxyhemoglobin to total hemoglobin ($0 \le SO_2 \le 100\%$) [20]. Similarly, the absorption coefficient of deoxy-hemoglobin is given by [51,57]

$$\mu_{a,deoxy}(\lambda) = \epsilon_{deoxy}(\lambda) C_{heme}(1 - SO_2)/66,500, \quad (41)$$

where ϵ_{deoxy} is the molar extinction coefficient of deoxyhemoglobin. Unlike the blood volume f_{blood} and oxygen saturation SO_2, which may vary from location to location and with metabolic state, the average value of $C_{heme} = 150\,\mathrm{g/liter}$ is typically used [51,58,59]. Furthermore, the molar extinction coefficients of oxyhemoglobin and deoxyhemoglobin for a wide range of wavelengths are available in the literature [51,60–63] and are reproduced in Fig. 8 in the visible range from 450 to 700 nm.

The transport scattering coefficient of biological media has been shown to follow a power law dependence on wavelength [64]:

$$\mu_{s,tr} = C_{tr}\lambda^k, \quad (42)$$

where λ is expressed in nanometers and $\mu_{s,tr}$ in cm^{-1}. For both epidermis and dermis, the values of C_{tr} and k were taken as $5.50 \times 10^5\,\mathrm{cm}^{-1}$ and -1.30, respectively [65]. The thickness of the epidermis on the hand and arm ranges between 50 and 130 μm [66]. The blood volume fraction and melanocyte volume fraction range from 0.2% to 7% and from 1% to 43%, respectively [52]. In this simulation, the epidermal thickness was taken as $L_1 = 100\,\mu$m. The epidermis and dermis were assumed to have the same index of refraction equal to 1.44 [24]. The blood volume and melanin concentrations were taken as $f_{blood} = 2.5\%$ and $f_{mel} = 1.0\%$, which are typical of healthy, lightly pigmented human skin [52].

Figure 9 shows the diffuse reflectance of human skin for $SO_2 = 0$ and 100% as predicted by Monte Carlo simulations and Eqs. (33)–(35) as a function of wavelength. For high values of SO_2, i.e., for highly oxygenated blood, the skin exhibits the absorption peaks of oxyhemoglobin around 542 and 580 nm. For low SO_2, or oxygen-depleted blood, the skin exhibits the single absorption peak of deoxy-hemoglobin near 560 nm. In both cases, the semiempirical model developed in this study agrees with Monte Carlo simulations within less than 8% relative error. The relative error is less than 3% for wavelengths between 525 and 600 nm, where absorption by oxyhemoglobin and deoxyhemoglobin is most distinct. Thus, the model can be used in diffuse reflectance spectroscopy for monitoring oxygenation and microcirculation of skin and wounds.

Figure 10 shows *in vivo* diffuse reflectance measurements from the top of the index finger of a healthy,

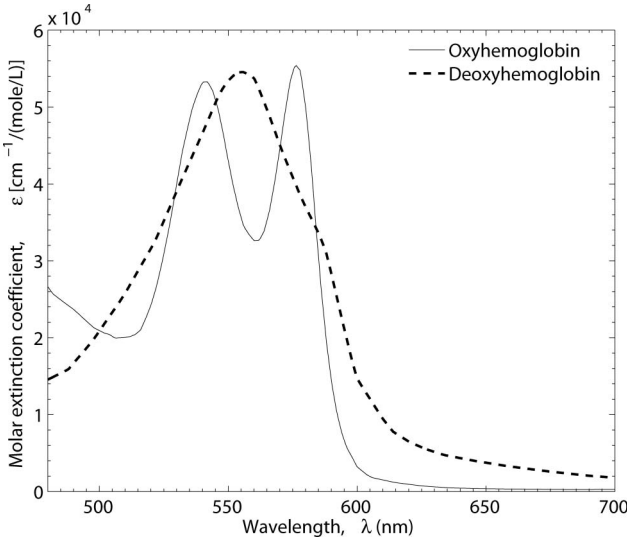

Fig. 8. Spectral molar extinction coefficient of human oxyhemoglobin and deoxyhemoglobin in the visible range (480 to 700 nm) [51].

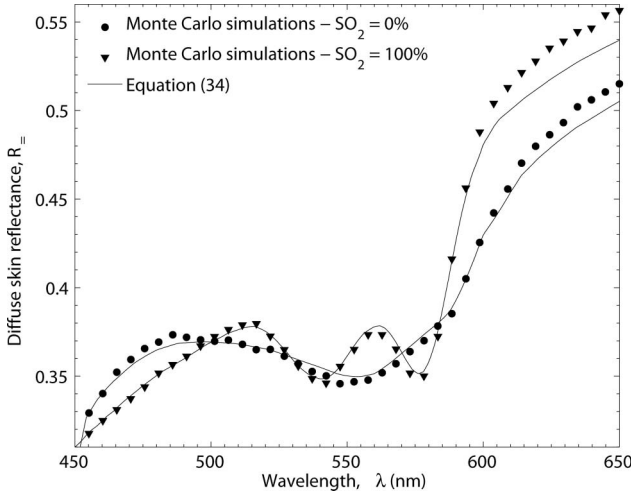

Fig. 9. Comparisons of diffuse reflectance of skin predicted by Monte Carlo simulations and by Eq. (34) as a function of wavelength for $f_{mel} = 1.0\%$, $f_{blood} = 2.5\%$, $L_1 = 100\,\mu$m, and $SO_2 = 0$ and 100%.

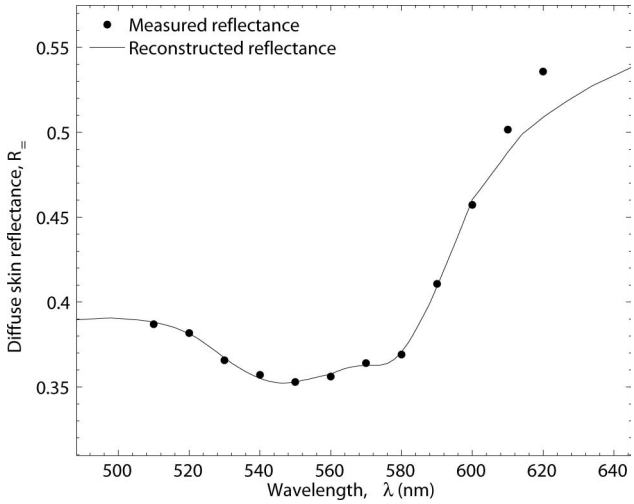

Fig. 10. Experimentally measured diffuse reflectance from the top of the index finger of a healthy, Caucasian subject along with reconstructed reflectance predicted by Eqs. (33)–(35) and Eqs. (36)–(42) with best-fit parameters $f_{mel} = 1.03\%$, $f_{blood} = 2.79\%$, $SO_2 = 29.0\%$ and $L_1 = 66\,\mu$m.

Caucasian male subject, along with a reconstruction of the same reflectance spectrum by the present model [Eqs. (33)–(35) and Eqs. (36)–(42)]. The reflectance spectrum was measured using a FDA approved hyperspectral camera (OxyVu, HyperMed Inc., Burlington, Massachusetts). The reconstruction was performed by minimizing the root mean square error between the observed and reconstructed diffuse reflectance while varying f_{mel}, f_{blood}, SO_2, and L_1. The Levenberg–Marquardt algorithm [67] was used to perform the nonlinear fit. The best-fit parameters found were $f_{mel} = 1.03\%$, $f_{blood} = 2.79\%$, and $SO_2 = 29.0\%$ and $L_1 = 66\,\mu$m. The SO_2 value predicted by the present method is in close agreement with the measurement obtained with OxyVu (28%) [20]. Furthermore, the retrieved value of f_{mel} was consistent with that of Caucasian skin [52] and the estimate of f_{blood} and L_1 fell within the range of physiologically realistic values [52,66]. Detailed discussion of the capability and robustness of the inverse method using the semiempirical model developed in this paper and application to hyperspectral imaging of human skin will be reported in a subsequent publication.

6. Conclusion

A model of diffuse reflectance was developed for nonemitting, absorbing, and scattering semi-infinite and two-layer media. Scattering was assumed to be strongly forward and to dominate over absorption. First, the two-flux approximation was used to find an approximate expression for the diffuse reflectance of a semi-infinite medium. Then, the coefficients of the expression were modified with numerical data from Monte Carlo simulations, resulting in a semiempirical model. Predictions from the semiempirical model agree with results from Monte Carlo simulations within 10% for $\omega_{tr} > 0.50$. This relative error decreases to less than 2% for $\omega_{tr} > 0.70$.

Similarly, an approximate reflectance $\tilde{R}_=$ and reduced reflectance $\tilde{R}^*$ were derived from the two-flux approximation of a two-layer medium. It was shown that $\tilde{R}^*$ is a function of the two-flux optical thickness Y_1 and parameter $\tilde{\alpha}$. To account for phenomena taking place at the medium/air interface, $\tilde{\alpha}$ was replaced by an empirical parameter α, which was fitted to match results from Monte Carlo simulations. Therefore, the reflectance of the two-layer medium could be expressed as a function of a single empirical parameter. The diffuse reflectance predicted by the semiempirical model fell within 10% of results from Monte Carlo simulations for $0.60 < \omega_{tr,1}$ and $0.60 < \omega_{tr,2}$ and the different values of n_1 and τ_1 considered in this study.

Finally, the semiempirical model for two-layer media was applied to lightly pigmented human skin with properties taken from the literature. The model developed in this study agrees with Monte Carlo simulations within 3% relative error for wavelengths between 480 and 650 nm.

Appendix A: Nomenclature

a,b	K-M dimensionless parameters
A_i,B_i	Single-layer model fit coefficients
C,D,E	Two-layer fit coefficients
C_{tr}	Scattering constant in Eq. (42)
F^-,F^+	Diffuse backward and forward fluxes, W/cm^2 · nm
g	Henyey–Greenstein asymmetry factor
I	Radiation intensity, W/cm^2 · sr · nm
I_0	Incident radiation intensity at the slab surface, W/cm^2 · sr · nm
I_r	Intensity of reflected light, W/cm^2 · sr · nm
k	Scattering constant in Eq. (42)
K	K-M effective absorption coefficient, 1/cm
L_1	Thickness of slab layer, cm
n_0	Index of refraction of the surroundings
$n_{1,2}$	Index of refraction of Layers 1 and 2
N	Polynomial order
q_0	Radiative flux of incident beam, W/cm^2 · nm
q_r	Backscattered radiative flux, W/cm^2 · nm
$\hat{r}$	Position vector, cm
R	Diffuse reflectance
R^*	Reduced reflectance
$\hat{s}$	Unit vector in a given direction
S	K-M effective scattering coefficient, 1/cm
SO_2	Oxygen saturation, %
Y	K-M optical thickness
z	Distance into the medium surface, cm

Greek symbols

α	Empirical fit coefficient of the two-layer reflectance model
β	Total extinction coefficient, 1/cm
η,χ	Parameters defined by Eq. (15)
θ	Polar angle, rad
θ_i	Angle of incidence on interface, rad
θ_t	Angle of transmitted radiation through interface, rad
θ_c	Critical angle for total internal reflection, rad
ϕ	Parameter defined by Eq. (17)
Φ	Scattering phase function, sr^{-1}
μ	Director cosine, $\mu = \cos\theta$
μ_a	Linear absorption coefficient, 1/cm
μ_s	Linear scattering coefficient, 1/cm
$\mu_{s,tr}$	Transport scattering coefficient [$= \mu_s(1-g)$], 1/cm
ω	Single-scattering albedo

ω_{tr}	Transport single-scattering albedo
Ω	Solid angle, sr
ρ_{01}	Specular reflectivity to normally incident light
ρ_{10}	Hemispherical–hemispherical reflectivity
$\rho''(\theta_i)$	Directional specular reflectivity
$\tau_{tr,1}$	Transport optical thickness of the slab layer

Subscripts

1	Refers to layer 1
2	Refers to layer 2
λ	Wavelength
$=$	Refers to two-layer medium
$-$	Refers to semi-infinite medium
back	Background
deoxy	Deoxyhemoglobin
d	Hemispherical–hemispherical reflectance with index matched boundary
oxy	Oxyhemoglobin

References

1. W. M. Kuebler, "How NIR is the future in blood flow monitoring?," J. Appl. Physiol. **104**, 905–906 (2008).
2. A. Torricelli, D. Contini, A. Pifferi, L. Spinelli, and R. Cubeddu, "Functional brain imaging by multi-wavelength time-resolved near infrared spectroscopy," Opto-Electron. Rev. **16**, 131–135 (2008).
3. G. Zonios, A. Dimou, I. Bassukas, D. Galaris, A. Tsolakidis, and E. Kaxiras, "Melanin absorption spectroscopy: new method for noninvasive skin investigation and melanoma detection," J. Biomed. Opt. **13**, 014017 (2008).
4. V. V. Tuchin, *Tissue Optics: Light Scattering Methods and Instruments for Medical Diagnosis* (SPIE, 2007).
5. L. Khaodhiar, T. Dinh, K. T. Schomacker, S. V. Panasyuk, J. E. Freeman, R. Lew, T. Vo, A. A. Panasyuk, C. Lima, J. M. Giurini, T. E. Lyons, and A. Veves, "The use of medical hyperspectral technology to evaluate microcirculatory changes in diabetic foot ulcers and to predict clinical outcomes," Diabetes Care **30**, 903–910 (2007).
6. R. L. P. van Veen, A. Amelink, M. Menke-Pluymers, C. van der Pol, and H. Sterenborg, "Optical biopsy of breast tissue using differential path-length spectroscopy," Phys. Med. Biol. **50**, 2573–2581 (2005).
7. U. Utzinger and R. R. Richards-Kortum, "Fiber optic probes for biomedical optical spectroscopy," J. Biomed. Opt. **8**, 121–147 (2003).
8. H. Huang, H. Yu, H. Xu, and Y. Ying, "Near infrared spectroscopy for on/in-line monitoring of quality in foods and beverages: a review," J. Food Eng. **87**, 303–313 (2008).
9. A. A. Gowen, C. P. O'Donnell, P. J. Cullen, G. Downey, and J. M. Frias, "Hyperspectral imaging–an emerging process analytical tool for food quality and safety control," Trends Food Sci. Technol. **18**, 590–598 (2007).
10. G. W. Heitschmidt, B. Park, K. C. Lawrence, W. R. Windham, and D. P. Smith, "Improved hyperspectral imaging system for fecal detection on poultry carcasses," Trans. Am. Soc. Agric. Biol. Eng. **50**, 1427–1432 (2007).
11. I. Kim, M. S. Kim, Y. R. Chen, and S. G. Kong, "Detection of skin tumors on chicken carcasses using hyperspectral fluorescence imaging," Trans. Am. Soc. Agric. Eng. **47**, 1785–1792 (2004).
12. N. Yamada and S. Fujimura, "Nondestructive measurement of chlorophyll pigment content in plant leaves from three-color reflectance and transmittance," Appl. Opt. **30**, 3964–3973 (1991).
13. M. J. D. van Gemert, and W. M. Star, "Relations between the Kubelka–Munk and the transport equation models for anisotropic scattering," Lasers Life Sci. **1**, 287–298 (1987).
14. D. Landgrebe, "Hyperspectral image data analysis," IEEE Signal Processi. Mag. **19**, 17–28 (2002).
15. E. S. Chalhoub and H. F. Campos Velho, "Simultaneous estimation of radiation phase function and albedo in natural waters," J. Quant. Spectrosc. Radiat. Transfer **69**, 137–149 (2001).
16. L. L. Richardson, "Remote sensing of algal bloom dynamics," BioScience **46**, 492–501 (1996).
17. R. Drezek, K. Sokolov, U. Utzinger, I. Boiko, A. Malpica, M. Follen, and R. Richards-Kortum, "Understanding the contributions of NADH and collagen to cervical tissue fluorescence spectra: Modeling, measurements, and implications," J. Biomed. Opt. **6**, 385–396 (2001).
18. G. I. Zonios, R. M. Cothren, J. T. Arendt, J. Wu, J. Van Dam, J. M. Crawford, R. Manoharan, and M. S. Feld, "Morphological model of human colon tissue fluorescence," IEEE Trans. Biomed. Eng. **43**, 113–122 (1996).
19. S. H. Tseng, A. Grant, and A. J. Durkin, "*In-vivo* determination of skin near-infrared optical properties using diffuse optical spectroscopy," J. Biomed. Opt. **13**, 014016 (2008).
20. K. J. Zuzak, M. D. Schaeberle, E. N. Lewis, and I. W. Levin, "Visible reflectance hyperspectral imaging: characterization of a noninvasive, *in-vivo* system for determining tissue perfusion," Anal. Chem. **74**, 2021–2028 (2002).
21. M. F. Modest, *Radiative Heat Transfer*, 2nd ed. (Academic, 2003).
22. M. J. C. van Gemert and W. M. Star, "Relations between the Kubelka-Munk and the transport equation models for anisotropic scattering," Lasers Life Sci. **1**, 98 (1987).
23. L. G. Henyey and J. L. Greenstein, "Diffuse radiation in the galaxy," Astrophys. J. **93**, 70–83 (1941).
24. M. J. C. Van Gemert, S. L. Jacques, H. Sterenborg, and W. M. Star, "Skin optics," IEEE Trans. Biomed. Eng. **36**, 1146–1154 (1989).
25. S. L. Jacques, C. A. Alter, and S. A. Prahl, "Angular dependence of HeNe laser light scattering by human dermis," Lasers Life Sci. **1**, 309–333 (1987).
26. K. Zhou, Z. Ren, S. Lin, H. Bao, B. Guo, and H. Y. Shum, "Real-time smoke rendering using compensated ray marching," in *Proceedings of the Association for Computing Machinery's Special Interest Group on Graphics and Interactive Techniques*, Vol. 1, pp. 1–12 (2008).
27. D. Q. Nguyen, R. Fedkiw, and H. W. Jensen, "Physically based modeling and animation of fire," in *Proceedings of the 29th Annual Conference on Computer Graphics and Interactive Techniques* (Association for Computing Machinery, 2002), pp. 721–728.
28. D. Calzetti, "The dust opacity of star-forming galaxies," Publ. Astron. Soc. Pac. **113**, 1449–1485 (2001).
29. J. M. Carvano, "Compositional interpretation of the geometric albedo of asteroids," Astron. Astrophys. **486**, 1031–1038 (2008).
30. S. Chandrasekhar, *Radiative Transfer* (Courier Dover, 1960).
31. P. Kubelka and F. Munk, "A contribution to the optics of pigments," Zeit. Technol. Phys. **12**, 593–599 (1931).
32. A. Schuster, "Radiation through a foggy atmosphere," Astrophys. J. **21**, 1–22 (1905).
33. P. Edström, "Examination of the revised Kubelka–Munk theory: considerations of modeling strategies," J. Opt. Soc. Am. **24**), 548–556 (2007).
34. J. L. Saunderson, "Calculation of the color of pigmented plastics," J. Opt. Soc. Am. **32**, 727–736 (1942).
35. W. E. Vargas and G. A. Niklasson, "Applicability conditions of the Kubelka–Munk theory," Appl. Opt. **36**, 5580–5586 (1997).
36. A. Gershun, "Fresnel reflection of diffusely incident light," J. Opt. Soc. Am. **35**, 162 (1945).

37. W. F. Cheong, S. A. Prahl, and A. J. Welch, "A review of the optical properties of biological tissues," IEEE J. Quantum Electron. **26**, 2166–2185 (1990).
38. G. Yoon, S. A. Prahl, and A. J. Welch, "Accuracies of the diffusion approximation and its similarity relations for laser irradiated biological media," Appl. Opt. **28**, 2250–2255 (1989).
39. S. L. Jacques, "Modeling tissue optics using Monte Carlo modeling: a tutorial," Proc. SPIE **6854**, 68540T (2008).
40. I. V. Meglinski and S. J. Matcher, "Modeling of skin reflectance spectra," Proc. SPIE **4241**, 78–87 (2001).
41. C. M. Gardner, S. L. Jacques, and A. J. Welch, "Light transport in tissue: accurate expressions for one-dimensional fluence rate and escape function based upon Monte Carlo simulation," Lasers Surg. Med. **18**, 129–138 (1996).
42. J. Wu, F. Partovi, M. S. Field, and R. P. Rava, "Diffuse reflectance from turbid media: an analytical model of photon migration," Appl. Opt. **32**, 1115–1121 (1993).
43. H. Zeng, C. E. MacAulay, B. Palcic, and D. I. McLean, "Monte Carlo modeling of tissue autofluorescence measurement and imaging," Proc. SPIE **2135**, 94–104 (1994).
44. I. Lux and L. Koblinger, *Monte Carlo Particle Transport Methods: Neutron and Photon Calculations* (CRC Press, 1991), p. 650.
45. L. Wang, S. L. Jacques, and L. Zheng, "MCML–Monte Carlo modeling of light transport in multi-layered tissues," Comput. Methods Programs Biomed. **47**, 131–146 (1995).
46. M. Keijzer, S. L. Jacques, S. A. Prahl, and A. J. Welch, "Light distributions in artery tissue: Monte Carlo simulations for finite-diameter laser beams," Lasers Surg. Med. **9**, 148–154 (1989).
47. G. M. Hale and M. R. Querry, "Optical constants of water in the 200 nm to 200 μm wavelength region," Appl. Opt. **12**, 555–563 (1973).
48. L. Wang and S. L. Jacques, "Monte Carlo modeling of light transport in multi-layered tissues in standard C," last accessed 31 March 2009, http://labs.seas.wustl.edu/bme/Wang/mcr5/Mcman.pdf.
49. S. L. Jacques, J. C. Ramella-Roman, and K. Lee, "Imaging skin pathology with polarized light," J. Biomed. Opt. **7**, 329–340 (2002).
50. K. M. Katika and L. Pilon, "Steady-state directional diffuse reflectance and fluorescence of human skin," Appl. Opt. **45**, 4174–4183 (2006).
51. S. Prahl, "Optical absorption of hemoglobin" (2002), http://omlc.ogi.edu/spectra/hemoglobin/hemestruct/index.html.
52. S. L. Jacques, "Origins of tissue optical properties in the UVA, visible, and NIR regions," in *Advances in Optical Imaging and Photon Migration*, R. R. Alfano and J. G. Fujimoto, eds. (Optical Society of America, 1996), Vol. 2, pp. 364–370.
53. I. S. Saidi, "Transcutaneous optical measurement of hyperbilirubinemia in neonates," Ph.D. dissertation (Rice University, 1992).
54. S. L. Jacques and D. J. McAuliffe, "The melanosome: threshold temperature for explosive vaporization and internal absorption coefficient during pulsed laser irradiation," Photochem. Photobiol. **53**, 769–775 (1991).
55. R. R. Anderson and J. A. Parrish, "The optics of human skin," J. Invest. Dermatol. **77**, 13–19 (1981).
56. M. J. C. Van Gemert, A. J. Welch, W. M. Star, M. Motamedi, and W. F. Cheong, "Tissue optics for a slab geometry in the diffusion approximation," Lasers Med. Sci. **2**, 295–302 (1987).
57. A. Krishnaswamy and G. V. G. Baranoski, "A biophysically-based spectral model of light interaction with human skin," in *Computer Graphics Forum* (Blackwell, 2004), Vol. 23, pp. 331–340.
58. A. N. Yaroslavsky, A. V. Priezzhev, J. R. I. V. Yaroslavsky, and H. Battarbee, "Optics of blood," in *Handbook of Optical Biomedical Diagnostics*, V. V. Tuchin, ed. (SPIE, 2002), pp. 169–216.
59. R. Flewelling, "Noninvasive optical monitoring," in *The Biomedical Engineering Handbook*, J. Bronzion, ed. (IEEE, 1981), pp. 1–11.
60. S. Wray, M. Cope, D. T. Delpy, J. S. Wyatt, and E. O. Reynolds, "Characterization of the near infrared absorption spectra of cytochrome aa3 and haemoglobin for the non-invasive monitoring of cerebral oxygenation.," Biochim. Biophys. Acta Bioenergetics **933**, 184–192 (1988).
61. A. P. Harris, M. J. Sendak, R. T. Donham, M. Thomas, and D. Duncan, "Absorption characteristics of human fetal hemoglobin at wavelengths used in pulse oximetry," J. Clin. Monit. Comput. **4**, 175–177 (1988).
62. S. Takatani and M. D. Graham, "Theoretical analysis of diffuse reflectance from a two-layer tissue model," IEEE Trans. Biomed. Eng. **bme-26**, 656–664 (1979).
63. O. W. Van Assendelft, *Spectrophotometry of Haemoglobin Derivatives* (Thomas, Springfield, 1970).
64. J. R. Mourant, J. P. Freyer, A. H. Hielscher, A. A. Eick, D. Shen, and T. M. Johnson, "Mechanisms of light scattering from biological cells relevant to noninvasive optical-tissue diagnostics," Appl. Opt. **37**, 3586–3593 (1998).
65. S. L. Jacques, "Skin optics," Oregon Medical Laser Center News **1998**, pp. 1–9 (1998).
66. Y. Lee and K. Hwang, "Skin thickness of Korean adults," Surg. Radiol. Anat. **24**, 183–189 (2002).
67. D. W. Marquardt, "An algorithm for least-squares estimation of nonlinear parameters," J. SIAM Control **11**, 431–441 (1963).